This article has been accepted for publication in IEEE Transactions on Neural Systems and Rehabilitation Engineering. This is the author's version which has not been fully edited and content may change prior to final publication. Citation information: DOI 10.1109/TNSRE.2026.3734253

SPAR-EEG: Selective Pass-Wise Artifact Reduction for Wearable Single-Channel EEG Denoising

Usman Qamar Shaikh[1,2], Anubha Manju Kalra[1,2], Andrew Lowe[1,3], and Imran Khan Niazi[4,5]

***Abstract*—Single-channel electroencephalography (EEG) is attractive for wearable neurotechnology and brain–computer interface (BCI) applications, including assistive interfaces and clinical monitoring, but artifact suppression is difficult when auxiliary channels, artifact labels, or user-selected clean baseline segments are unavailable. We introduce SPAR-EEG, a self-contained framework for Selective Pass-wise Artifact Reduction in single-channel EEG. The framework applies three artifact-specific attenuation passes to each EEG epoch: a variational mode decomposition (VMD)-based pass for high-frequency electromyographic (EMG) bursts, a singular spectrum analysis (SSA)-based pass for blink-like electrooculographic (EOG) transients, and an SSA-based pass for slow motion-related drift. Rather than rejecting components globally, each pass estimates artifact-dominant regions and attenuation strength directly from the input channel. SPAR-EEG was evaluated using controlled EEGdenoiseNet and PhysioBank benchmarks, pass ablations, task-locked event-related potential (ERP) preservation, runtime diagnostics, dry-electrode exercise EEG, and a downstream rapid serial visual presentation (RSVP)/P300 speller task using only FP1 and FP2. Across 26 EEGdenoiseNet input signal-to-noise ratio (SNR) levels, it obtained the largest average artifact-region SNR improvement among the tested wavelet, empirical mode decomposition (EMD), and artifact-label-guided wavelet quantile normalization (WQN) baselines for EMG, EOG, and combined EOG+EMG contamination (9.05, 8.28, and 8.00 dB, respectively). In exercise EEG, denoising reduced high-amplitude artifact burden and increased alpha and steady-state visual evoked potential (SSVEP) spectral-prominence metrics. In the P300 validation, the full SPAR-EEG sequence increased repetition-curve area under the curve (AUC) by 0.048 (Holm-adjusted $p = 0.0069$) and improved final Letter@15 accuracy by 7.8 percentage points. These results suggest that artifact-specific selective attenuation can provide a practical self-contained alternative for single-channel EEG denoising in low-burden and movement-prone settings.**

***Index Terms*—Electroencephalography (EEG), EEG artifact removal, single-channel EEG, wearable neurotechnology, brain-computer interfaces (BCI).**

I. Introduction

Electroencephalography (EEG) provides millisecond-scale access to brain dynamics and remains central to brain-computer interfaces (BCIs), clinical monitoring, neurorehabilitation, and cognitive-state assessment [1]. In parallel, wearable and reduced-lead EEG systems lower setup burden and support low-supervision recordings for assistive BCI, home rehabilitation monitoring, and single-channel applications [2]. This shift also makes artifact suppression more constrained: when only one or a few channels are available, the signal-processing pipeline has less spatial redundancy and fewer auxiliary measurements from which to distinguish neural and non-neural activity.

The constraint is important because EEG is readily contaminated by ocular activity, cranial and facial electromyographic (EMG) activity, motion/contact disturbances, slow baseline drift, and environmental noise. Ocular potentials can propagate broadly across the scalp [3], blink artifacts can overlap low-frequency neural activity [4], and muscular artifacts can be broadband and spatially diffuse [5]. These problems become especially consequential in portable or dry-electrode settings where signal quality varies over time and quality-control decisions may need to be made automatically [6].

Established artifact-correction methods are powerful when their assumptions are satisfied. Independent component analysis and spatial projection/subspace approaches exploit multichannel structure to separate or suppress artifact-related activity [7]–[9], while regression and adaptive-filtering methods can reduce ocular contamination when suitable reference channels or artifact measurements are available [10], [11]. However, these assumptions are not generally available in EEG-only single-channel deployment. A single recording channel cannot provide the same spatial mixture information as a multichannel montage, and adding dedicated EOG or EMG references can conflict with the low-burden design goals of wearable systems.

Recent deep learning methods have produced strong benchmark results for single-channel EEG denoising. Transformer-based models and GAN-guided CNN-transformer hybrids learn nonlinear mappings from contaminated to clean EEG and are commonly trained and evaluated on semi-simulated mixtures such as EEGdenoiseNet [12]–[14]. These models are valuable because they can learn complex temporal structure beyond hand-designed thresholds. Their limitations are complementary to their strengths: they are typically trained as always-on waveform reconstructors, their behavior is governed largely by the training distribution, and they offer fewer explicit handles for artifact-type-specific attenuation, selective pass-through of weakly contaminated epochs, or application-specific control of latency and aggressiveness.

Decomposition-based methods offer a more interpretable alternative because they expose intermediate coefficients, modes, or components that can be inspected and selectively modified.

Corresponding author: Imran Khan Niazi (e-mail: imran.niazi@nzchiro.co.nz). [1]Institute of Biomedical Technologies, Auckland University of Technology, Auckland, New Zealand. [2]Electrical and Electronic Engineering Department, Faculty of Engineering, Computer and Mathematical Sciences, Auckland University of Technology, Auckland, New Zealand. [3]Mechanical Engineering Department, Faculty of Engineering, Computer and Mathematical Sciences, Auckland University of Technology, Auckland, New Zealand. [4]Centre for Chiropractic Research, New Zealand College of Chiropractic, Auckland, New Zealand. [5]Department of Health Science and Technology, Aalborg University, Aalborg, Denmark. ORCID iDs: U.Q.S., 0009-0000-0171-3940; A.M.K., 0000-0001-7908-3053; A.L., 0000-0002-0612-1036; I.K.N., 0000-0001-8752-7224.

In the wavelet family, thresholding methods use multiresolution coefficients to suppress high-amplitude time-frequency content, but their performance depends on the wavelet basis, decomposition level, and threshold rule [15], [16]. More structured wavelet approaches have used discrete wavelet coefficients to construct an internal ocular-artifact reference for adaptive noise cancellation [17], or estimated an artifact probability before applying stationary-wavelet cleaning in BCI-oriented single-channel data [18]. SuBAR generates surrogate signals to estimate stationary wavelet-domain structure and then suppresses coefficients in the observed signal that exceed surrogate-derived thresholds [5]. WQN is also particularly relevant because it renormalizes wavelet-coefficient distributions in artifact segments using adjacent uncontaminated signal as a reference distribution [19]; in its validation, artifact segmentation is treated as known input, separating coefficient normalization from artifact detection and baseline selection.

EMD and CEEMDAN variants adaptively decompose nonstationary signals into intrinsic modes [20], [21]. Several single-channel methods use these modes as a derived multichannel representation: EEMD-CCA and EEMD-ICA use second-order or independent-component structure after decomposition [22], [23], EEMD-MCCA has been used for single-channel muscle-artifact removal [24], and CEEMDAN-ICA-WTD or CEEMDAN-BD variants have been proposed for ocular-artifact correction while avoiding complete deletion of EEG-containing artifact components [25], [26]. These transformed single-channel hybrids are important precedents because they make blind-source-separation-like processing possible from one channel. Their practical behavior, however, remains tied to mode mixing, boundary effects, decomposition length, and the rules used to identify artifact-dominant modes or components.

VMD was introduced to obtain compact narrowband modes with estimated center frequencies [27]. This property has motivated VMD-SOBI for single-channel EOG/EMG removal [28], two-stage VMD frameworks for ocular-artifact detection and removal [29], [30], and VMD-CCA or VMD-PCA pipelines for motion-artifact correction [31]. These studies show that VMD is a powerful decomposition family for single-channel artifact handling, especially when narrowband structure is informative. However, the artifact-selection logic must still be matched to the artifact morphology: high-frequency burst artifacts are naturally compatible with frequency-organized modes, whereas sharp blink-like transients may be distributed across modes rather than isolated as a single narrowband source.

SSA-based approaches provide a complementary route because the trajectory-matrix representation can separate components by waveform structure and amplitude patterns. This is especially attractive for ocular artifacts: k-means and SSA have been used to estimate blink artifacts and reduce modification of uncontaminated regions [4]. SSA has also been combined with SOBI/ICA-style separation for simultaneous EMG, EOG, and ECG removal [32], and with ICA and total-variation filtering to remove multi-artifact mixtures while preserving neural residue within artifact components [33]. These works demonstrate that single-channel methods need not be limited to one artifact family, but much of the evidence remains semi-simulated or dependent on artifact-component selection, with comparatively limited validation using downstream neural outcomes. Prior work on single-channel artifact-load estimation also supports treating ocular and muscular contamination as distinct processes rather than as one generic noise source [34]. These considerations are especially relevant in long or weakly supervised recordings, where artifact annotation, reference noise channels, and user-selected clean baseline segments may be impractical. They motivate testing a self-contained, artifact-specific strategy in which the attenuation rule is matched to the targeted artifact morphology.

In this work, we propose SPAR-EEG, a self-contained framework for Selective Pass-wise Artifact Reduction in single-channel EEG. Its principal algorithmic contribution is a baseline-referenced component-region attenuation strategy: a cross-component envelope proxy locates candidate artifact intervals, component-specific envelopes shape local masks, and regularized optimization reduces artifact-region energy toward the component's within-window baseline without rejecting the complete component. A nonlinear gain distributes this attenuation smoothly in time. Artifact-specific VMD and SSA passes operationalize this mechanism for high-frequency EMG bursts and blink-like ocular transients, while a separately gated SSA pass treats sustained slow drift. SPAR-EEG estimates artifact regions and attenuation strengths from the observed channel without externally supplied intervals, reference channels, or baseline segments. We evaluate the framework against guided and unguided single-channel baselines, characterize pass interaction and task-locked ERP preservation, and examine spectral and event-related EEG usability using a public RSVP/P300 dataset [35].

The main contributions of this paper are:

- a baseline-referenced component-region attenuation rule that retains artifact-bearing components and regularizes only their detected artifact-dominant intervals, implemented within a self-contained artifact-specific three-pass framework;
- a controlled benchmark on ground-truth artifact mixtures derived from public datasets, comparing the self-contained SPAR-EEG pipeline with unguided wavelet thresholding and guided WQN, EMD-CCA, and EMD-ICA baselines;
- ablation, parameter-sensitivity, artifact-geometry, task-locked ERP-preservation, adaptive-streaming, and computational-cost analyses that characterize the behavior and limitations of the SPAR-EEG passes;
- task-oriented validation in dry-electrode exercise EEG using alpha and steady-state visual evoked potential (SSVEP) spectral-prominence metrics; and
- downstream event-related validation in a public RSVP/P300 speller dataset using a common SWLDA protocol with separately fitted subject models for each preprocessing branch and only FP1/FP2 channels [35].

The remainder of this paper is organized as follows. Section II defines the SPAR-EEG three-pass denoising algorithm. Section III describes the benchmark datasets, application

This article has been accepted for publication in IEEE Transactions on Neural Systems and Rehabilitation Engineering. This is the author's version which has not been fully edited and content may change prior to final publication. Citation information: DOI 10.1109/TNSRE.2026.3734253

datasets, comparison methods, metrics, and statistical analyses. Section IV presents the benchmark, diagnostic, exercise EEG, and P300 validation results. Sections V and VI discuss the findings and summarize the main conclusions.

II. SPAR-EEG ALGORITHM

This section defines the SPAR-EEG epoch-level pipeline, then details the shared attenuation principle and artifact-specific EMG, EOG, and slow-drift passes.

Let

$$\mathbf{y} = [y[1], y[2], \ldots, y[T]]^{\mathsf{T}} \in \mathbb{R}^T \tag{1}$$

denote a single-channel EEG epoch with T samples, acquired at sampling frequency F_s. The cleaned epoch is obtained by applying three artifact-specific passes sequentially:

$$\hat{\mathbf{y}} = \mathcal{D}_{\text{slow}}(\mathcal{D}_{\text{EOG}}(\mathcal{D}_{\text{EMG}}(\mathbf{y}; F_s); F_s)\,; F_s)\,, \tag{2}$$

where $\mathcal{D}_{\text{EMG}}$, $\mathcal{D}_{\text{EOG}}$, and $\mathcal{D}_{\text{slow}}$ denote the EMG, EOG, and slow-drift pass operators, respectively, and $\hat{\mathbf{y}}$ is the cleaned epoch.

Figure 1 summarizes the pass sequence and the distinct role of each module.

The method is defined at the epoch level and is applied directly to fixed-length datasets such as EEGdenoiseNet or ERP/SSVEP epochs. For continuous recordings, adaptive streaming first partitions the signal into 2–4 s windows whose boundaries are selected at comparatively stable samples before applying the same epoch-level passes.

The design principle is artifact-specific component-region attenuation. Rather than classifying and rejecting a complete component, the EMG and EOG passes identify temporally abnormal portions within artifact-relevant components and retain those components after local treatment. High-frequency muscle bursts, blink-like ocular transients, and broad low-frequency motion drifts are treated by different mechanisms because they occupy different decomposition subspaces and temporal supports.

A. Shared Selective Attenuation Structure

The EMG and EOG passes follow a common selective attenuation structure. First, the input epoch is robustly normalized. In the default implementation, the scale is estimated using the median absolute deviation (MAD),

$$\begin{aligned} s &= \mathrm{MAD}(\mathbf{y}) + \delta, \\ \tilde{\mathbf{y}} &= \frac{\mathbf{y}}{s}, \end{aligned} \tag{3}$$

where s is the robust scale of the current pass input and δ is a small scale floor. Each pass performs decomposition and attenuation in normalized coordinates and then rescales the cleaned signal back to the input units. The normalized epoch is decomposed into components, an artifact proxy is built from components expected to express the target artifact, and the proxy is smoothed and robustly z-scored. Samples whose proxy amplitude exceeds a threshold are expanded by fixed temporal dilation and smoothing to obtain a soft common artifact mask. Contiguous suprathreshold intervals are retained as artifact regions only when their duration exceeds a minimum artifact length.

Within each detected region r, the envelope of component k defines a soft component-specific mask $m_{k,r}[n] \in [0, 1]$. Thus, the common proxy determines where a candidate artifact occurs, whereas the component envelope determines how its temporal support is expressed within each component. A scalar attenuation coefficient $a_{k,r} \in [a_{\min}, 1]$ is optimized separately for every component-region pair, with $a_{\min}$ defining the maximum allowed attenuation. The objective compares post-attenuation energy in artifact-dominant samples with energy in the within-window baseline:

$$J(a) = \left[\log \frac{E_{\text{art}}(a) + \varepsilon}{E_{\text{base}}(a) + \varepsilon}\right]^2 + \lambda(1 - a)^2. \tag{4}$$

Here $E_{\text{art}}(a)$ and $E_{\text{base}}(a)$ are the attenuated mean-square component energies over the artifact and baseline samples, ε is a small positive constant used for numerical stability, and λ penalizes departure from the identity gain $a = 1$. The first term therefore regularizes artifact-region energy toward the local baseline instead of minimizing output energy without constraint.

The optimized coefficient is converted to the time-varying gain

$$\begin{aligned} \gamma(a_{k,r}) &= \min\left(1, \frac{\eta a_{k,r}}{1 - a_{k,r} + \varepsilon}\right), \\ w_{k,r}[n] &= 1 - (1 - a_{k,r})\big(m_{k,r}[n]\big)^{\gamma(a_{k,r})}, \end{aligned} \tag{5}$$

where η controls gain shaping. For stronger optimized attenuation, the exponent broadens the reduction over the detected component-region support instead of concentrating it only at the envelope maximum. Gains from overlapping regions are multiplied, and all attenuated and unchanged components remain in the reconstruction. This differs from hard rejection or uniform attenuation of the complete component.

B. VMD-Based EMG Burst Suppression

The EMG pass targets localized high-frequency myogenic bursts. It assumes that the epoch contains both artifact-dominant samples and relatively clean baseline samples. If the entire epoch is dominated by EMG activity, the baseline-referenced attenuation objective in (4) becomes less informative.

VMD is used in this pass because its modes are narrowband by construction [27]. This property makes it feasible to identify and treat higher-frequency modes associated with muscle activity while leaving lower-frequency EEG-dominant modes largely unaffected. The normalized epoch is decomposed as

$$\tilde{\mathbf{y}} \to \{u_k[n]\}_{k=1}^{K}, \tag{6}$$

where $u_k[n]$ is the kth VMD mode and K is the number of modes in this pass. Modes are sorted by spectral centroid. A high-frequency set $\mathcal{K}_{\text{HF}}$ is selected for artifact proxy construction. For each selected mode, the analytic envelope is computed as

$$e_k[n] = \left|\mathcal{H}\{u_k[n]\}\right|, \tag{7}$$

This article has been accepted for publication in IEEE Transactions on Neural Systems and Rehabilitation Engineering. This is the author's version which has not been fully edited and content may change prior to final publication. Citation information: DOI 10.1109/TNSRE.2026.3734253

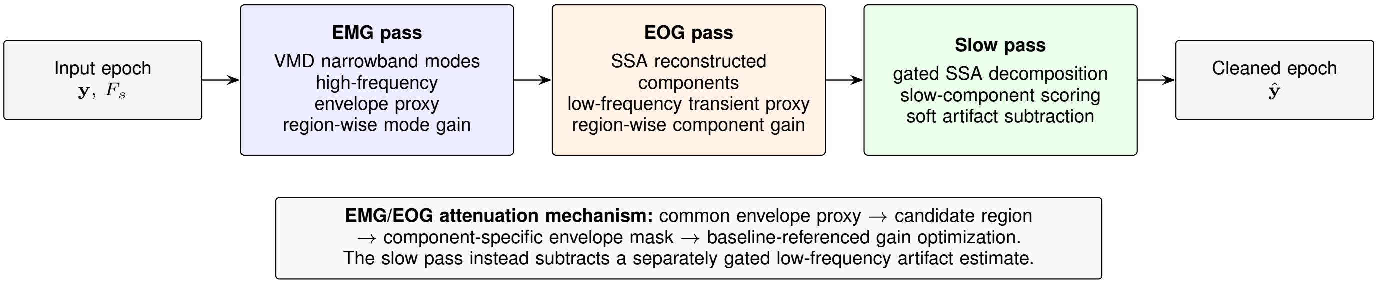

Fig. 1. Flowchart of the SPAR-EEG artifact-specific single-channel EEG denoising pipeline. The three deployed passes share the same selective-denoising principle but use artifact-specific decompositions, proxies, gates, and attenuation operations. The detailed active flow and representative pass internals are provided in Supplementary Section II, Supplementary Table I, and Supplementary Figs. 1–3.

where $\mathcal{H}\{\cdot\}$ denotes the Hilbert transform. The EMG proxy is

$$p_{\mathrm{EMG}}[n] = \mathrm{median}_{k\in\mathcal{K}_{\mathrm{HF}}} e_k[n]. \tag{8}$$

Median aggregation reduces sensitivity to a single unstable mode and emphasizes burst activity appearing across the high-frequency subspace.

The proxy $p_{\mathrm{EMG}}[n]$ is smoothed, robustly z-scored, thresholded, dilated, and converted into candidate burst regions. For each burst region and each treatable VMD mode, clean baseline samples are explicitly protected by setting the attenuation mask to zero where the common artifact mask is below the baseline threshold. The optimized gains are then applied to the VMD modes, the attenuated modes are summed, and the returned pass output is rescaled to the input units.

C. SSA-Based Ocular Artifact Suppression

The EOG pass targets blink-like ocular transients that are sparse in time and typically appear as high-amplitude structured waveforms. Like the EMG pass, it benefits from the presence of baseline samples within the epoch. SSA is used instead of VMD because ocular transients are not reliably represented as a single narrowband component, consistent with prior SSA-based blink-removal work [4]. Sharp blinks or spike-like ocular events can be distributed across several VMD modes, making frequency-based suppression less direct. SSA is more shape-driven because it decomposes the trajectory matrix into reconstructed components that can capture dominant temporal structures.

The normalized input to the EOG pass is embedded into a Hankel trajectory matrix, singular value decomposition is applied, and each rank-one matrix is mapped back to a time series using diagonal averaging. The resulting reconstructed components $c_k[n]$ are sorted by spectral centroid. A low-frequency component set $\mathcal{K}_{\mathrm{LF}}$ is selected and an ocular proxy is formed from the median Hilbert envelope:

$$p_{\mathrm{EOG}}[n] = \mathrm{median}_{k\in\mathcal{K}_{\mathrm{LF}}} \left|\mathcal{H}\{c_k[n]\}\right|. \tag{9}$$

The ocular proxy is processed using the same region-detection logic as the EMG proxy: smoothing, robust z-scoring, thresholding, temporal dilation, and minimum-duration filtering. For each detected ocular region and each treated SSA component, the algorithm constructs a component-specific soft mask and optimizes an attenuation coefficient using (4). The attenuated components are summed and rescaled to the input units. Thus, the EOG pass shares the selective attenuation principle with the EMG pass, but replaces narrowband VMD separation with shape-sensitive SSA decomposition.

D. SSA-Based Slow-Drift Suppression

The slow-drift pass targets broad low-frequency motion artifacts, electrode displacement, and baseline sway. Unlike the EMG and EOG passes, it neither partitions the epoch into local artifact and baseline regions nor applies component-specific regional gains. Because slow contamination may occupy most or all of an epoch, the module instead uses epoch-level gates and softly subtracts a single SSA-derived low-frequency artifact estimate without requiring a clean within-window interval.

A first-stage gate determines whether slow-artifact processing is needed before running SSA. In the default implementation, this gate is driven by the ratio of low-frequency power to total epoch power. If the low-frequency ratio does not exceed the gate threshold, the epoch bypasses the slow-drift pass unchanged. This bypass limits unnecessary SSA-based subtraction in epochs without clear slow-drift evidence.

If the first gate passes, SSA is applied and reconstructed components are sorted by spectral centroid. Candidate slow components are restricted to the low-frequency range and scored according to variance share, robust peak-to-peak contribution, and correlation with a smoothed trend. A weighted slow-artifact estimate is formed from the selected components, and a second-stage gate confirms that this estimate explains a meaningful portion of the epoch. When both gates pass, the estimate is subtracted with strength α selected by grid search over a bounded interval. The objective favors reduced low-frequency power, reduced robust peak-to-peak amplitude, controlled slope behavior, reduced residual correlation with the estimated artifact, and limited deviation from the input.

E. Sequential Application

The implemented order is EMG, EOG, and slow drift. High-frequency EMG bursts are first reduced using frequency-organized VMD modes, limiting their influence on subsequent transient analysis. Blink-like ocular artifacts are then attenuated using morphology-sensitive SSA components. Finally, the slow-drift pass considers broad low-frequency contamination after sharper burst-like artifacts have been reduced. Ablation assessed the contribution of each pass within this mechanistically motivated sequence; alternative pass permutations were not evaluated. The resulting pipeline treats multiple artifact morphologies without requiring reference channels or multichannel spatial information.

F. Application to Continuous Recordings

For continuous recordings, adaptive non-overlapping streaming segmentation selects stable 2–4 s windows before the epoch-level passes are applied. Boundary cost is defined by low amplitude, low slope, low local RMS energy, and a zero-crossing preference, so that each window tends to begin and end near locally stable signal levels. This reduces abrupt endpoint discontinuities and associated decomposition edge effects in long recordings while leaving fixed-length benchmark epochs unchanged.

III. Experimental Protocol

The experimental protocol contained three validation layers: controlled ground-truth and reference-signal benchmarks against established single-channel denoisers, a dry-electrode exercise EEG stress test of spectral neural-response preservation, and a public P300 speller validation of downstream event-related utility. Supporting diagnostics quantified pass interaction, task-locked ERP preservation, computational cost, and adaptive streaming behavior.

A. Benchmark Datasets and Preparation

EEGdenoiseNet: EEGdenoiseNet was used as the primary controlled benchmark. Clean EEG epochs were mixed with EOG, EMG, or combined EOG+EMG artifacts. For each artifact type, 3400 two-second epochs were generated at $F_s = 256$ Hz. Artifacts were injected into the middle third of each epoch so that clean samples remained on both sides. For each artifact type, 26 integer nominal input SNR levels were generated:

$$\mathrm{SNR}_{\mathrm{in}} \in \{-20, -19, \ldots, 0, 1, \ldots, 5\} \text{ dB}. \tag{10}$$

The artifact amplitude was scaled so that the SNR measured inside the artifact interval matched the nominal value for each epoch, yielding 78 EEGdenoiseNet H5 files.

The same 3400 unique clean EEG, EOG, and EMG source segments were reused across SNR levels and the relevant single- and mixed-artifact conditions. Segment-to-participant identifiers were not available in the released arrays; source counts and reuse are detailed in Supplementary Section VIII.

PhysioBank motion artifact dataset: The benchmark paired a stationary FPz reference with neighboring FP1h, whose lead was periodically pulled to induce motion artifact while participants remained still with their eyes closed [36]. Following the WQN preparation [19], 22 records were filtered from 0.1–100 Hz and resampled from 2048 to 256 Hz. Artifact intervals were derived from the smoothed FP1h–FPz discrepancy constrained by the acquisition motion trigger; neither FPz nor the intervals were supplied to SPAR-EEG. Exact exclusions, mask construction, and comparator guidance are provided in Supplementary Section II-C.

B. Exercise EEG Application Dataset

Application-oriented validation used dry-electrode EEG from 18 participants collected with an OpenBCI Cyton system at $F_s = 250$ Hz and stored through Lab Streaming Layer/LabRecorder. The study was approved by the Auckland University of Technology Ethics Committee (AUTEC application 24/325; approved 13 November 2025), and all participants provided informed consent. Recordings were converted from XDF to EEGLAB SET format and processed in paired form. The FIR baseline used EEGLAB Hamming-window filters: a 0.5–70 Hz band-pass (order 1650) followed by a 45–55 Hz band-stop filter (order 414), both implemented as one-pass zero-phase/noncausal FIR filtering by group-delay compensation. The SPAR-EEG adaptive three-pass pipeline was applied to O1 and O2.

All recorded EEG derivations used FP1 as the acquisition reference, making O1/O2 sensitive to frontal blink and ocular activity; FP1 itself was not stored independently. In the wearable-style condition, the Cyton ground/bias connection was placed at the earlobe. In the ground-assisted condition, an ESD wrist strap was additionally connected through a relay and Arduino ground to the plugged-in computer ground. Because the FP1 signal was unavailable, the original FP1-independent O1/O2 potentials or a physically neutral reference could not be reconstructed; rereferencing among the recorded channels would define a different montage.

Data were collected during eyes-open/eyes-closed alpha blocks and SSVEP stimulation at 6, 7.5, 8.57, and 10 Hz under rest and exercise conditions. The exercise tasks included rest, seated and standing marching, head movement, chewing, scalp scratching, mixed movement, and treadmill walking under ground-assisted and/or wearable-style acquisition. Detailed processing parameters, task coverage, and task descriptions are provided in Supplementary Section III-A and Supplementary Tables VII–IX. For the main summary, stable 2–4 s adaptive windows were processed with the EMG, EOG, and slow-drift sequence. For each participant and preprocessing branch, 4-s epoch PSDs were averaged within each exercise/acquisition-condition–channel item and then equally across the available items, yielding one collapsed PSD per alpha state or SSVEP frequency. Spectral metrics and paired SPAR-minus-FIR differences were calculated from these participant-level PSDs; PTP burden was calculated separately as the percentage of eligible O1/O2 epochs exceeding 150 μV within each participant and branch.

C. P300 BCI Downstream Validation

Downstream event-related validation used the public RSVP/P300 speller dataset of Won *et al.* [35]. FP1 and FP2 were used for all 55 participants to test a constrained, artifact-prone frontal montage relevant to low-burden assistive and rehabilitation-oriented BCI settings. The two calibration runs were used for training and the four test runs for evaluation. FP1/FP2 signals first underwent the shared wide conditioning used for all branches: MNE Hamming-window zero-double-phase FIR filtering from 0.5–70 Hz followed by a 50 Hz FIR notch (3381 taps for each filter; reflect-limited record-edge padding). Four preprocessing conditions were evaluated: wide-conditioned baseline, EOG-pass output, EMG+EOG output, and the full EMG+EOG+slow sequence.

The decoder protocol, training/test split, and hyperparameters were held fixed across preprocessing conditions, while a separate subject-specific SWLDA-style linear model was fitted for every preprocessing branch. Following the original dataset style and previous FP1/FP2 analysis [34], each continuous branch was demeaned and filtered from 0.5 to 10 Hz using a Butterworth design with $N = 4$ (four second-order sections) applied forward and backward. Signals were epoched from 0 to 600 ms after stimulus onset, baseline corrected using the -200 to 0 ms prestimulus interval, average-decimated by a factor of 24, and decoded by accumulating row and column scores over repetitions. Continuous denoising used contiguous adaptive windows processed independently without overlap or cross-fading; the first bootstrap window was retained unchanged. Filter transitions, padding, and segment-edge behavior are detailed in Supplementary Table XIII.

D. EEGLAB Sample Dataset for ERP Preservation

Task-locked preservation was examined using the public EEGLAB sample recording [37]. Independent preparation using 0.5–40 Hz FIR filtering, extended ICA, ICLabel-based eye/muscle component rejection, EOG-channel removal, and average rereferencing yielded 80 stimulus-locked trials over 30 channels [38]. The frozen EMG, EOG, EMG+EOG, and full configurations were applied to every channel and trial. Preservation was quantified using mean amplitude, analytic standardized measurement error (aSME), and SME-based ERP SNR [39], [40]; complete methods and branch-wise results are provided in Supplementary Section VI.

E. Comparison Methods and Supporting Diagnostics

The comparison methods were WQN, hard and soft wavelet thresholding, EMD-CCA, and EMD-ICA. Hard and soft wavelet thresholds were applied within the supplied artifact intervals. WQN was evaluated as artifact-label-guided because its benchmark implementation normalizes wavelet-coefficient distributions inside labeled artifact intervals using temporally adjacent uncontaminated EEG as a reference distribution [19]. The EMD-CCA and EMD-ICA benchmark implementations were reference-guided because source suppression was selected according to improvement in correlation to the reference signal. All comparison methods used the implementation style and default settings from the WQN benchmark repository wherever applicable, and restored outputs were scored using a common evaluation script. The experimental comparator set was limited to these implemented methods; modern neural denoisers were not experimentally evaluated.

For PhysioBank, SPAR-EEG used the slow-drift pass; for all EEGdenoiseNet conditions, the full practical sequence EMG, EOG, and slow drift was applied. The contribution of individual passes was examined on the EEGdenoiseNet -10 dB files using EMG only, EOG only, slow only, EMG+EOG, and full configurations. Computation cost was measured on the EEGdenoiseNet -10 dB files after data loading, excluding H5 writing, metric computation, plotting, and MATLAB startup. All methods were timed on the same workstation; the hardware, software, warm-up, and repeat protocol are reported in Supplementary Section II-E. Adaptive streaming behavior was summarized on PhysioBank by reporting the window lengths selected by the 2–4 s boundary policy. Detailed diagnostic settings and summaries are provided in Supplementary Section II.

Artifact-geometry robustness was evaluated using the same 500 paired EEGdenoiseNet EMG records at -10 dB artifact-region input SNR. The clean EEG and EMG carrier were held common across centered, random, left-edge, right-edge, three-burst, and full-epoch variants. A separate centered sweep varied artifact occupancy from 1/9 to 9/9 while preserving the -10 dB SNR within each artifact region. The synthesis masks were used only to construct and score the mixtures and were not supplied to SPAR-EEG. Complete results are reported in Supplementary Section VII.

F. Parameter Development and Sensitivity

The active defaults were established before formal evaluation through morphology-guided inspection of a small exploratory set of laboratory pilot waveforms. The exact pilot identities were not retained; some may have been EEGdenoiseNet-derived, so source-epoch overlap with the final source pool cannot be excluded. These pilots were not the centered mixtures later generated using the adapted WQN workflow. No aggregate results from the formal benchmark or data from PhysioBank, exercise EEG, RSVP/P300, or the EEGLAB ERP recording were used for parameter selection. The defaults were then frozen for all reported evaluations; Supplementary Section VIII summarizes development and evaluation provenance.

A post-freeze sensitivity analysis used a reproducibly sampled subset of 500 paired record IDs drawn from the final 3400-record EEGdenoiseNet source pool at artifact-region input SNRs of -20, -10, and 0 dB. One-factor-at-a-time analyses varied the VMD mode count ($K = 4, 8, 12$), SSA embedding length ($L = 4, 8, 12$ samples), EMG/EOG artifact-proxy threshold ($z_{\mathrm{thr}} = 1$–5), and no/submitted/doubled temporal dilation, while all other settings remained fixed. Artifact-region $\Delta\mathrm{SNR}$ was interpreted jointly with outside-mask output-change RRMSE, whole-epoch reconstruction error, activation or bypass behavior, and runtime. Alternatives were compared with the submitted setting using paired two-sided Wilcoxon tests with Holm adjustment within each pass, contamination level, and metric. Complete settings and outcomes are reported in Supplementary Section V.

G. Evaluation Metrics

The primary ground-truth metric was artifact-region SNR improvement:

$$\Delta\mathrm{SNR} = \mathrm{SNR}_{\mathrm{after}} - \mathrm{SNR}_{\mathrm{before}}, \tag{11}$$

where

$$\mathrm{SNR} = 10 \log_{10} \frac{\sum_n x^2[n]}{\sum_n (\hat{x}[n] - x[n])^2 + \varepsilon}. \tag{12}$$

This article has been accepted for publication in IEEE Transactions on Neural Systems and Rehabilitation Engineering. This is the author's version which has not been fully edited and content may change prior to final publication. Citation information: DOI 10.1109/TNSRE.2026.3734253

Here $x[n]$ is the clean or reference EEG, $\hat{x}[n]$ is the evaluated signal, and ε is a numerical stability constant. For EEGdenoiseNet, $\mathrm{SNR}_{\mathrm{before}}$ was set to the known nominal input SNR for each generated file.

Exercise EEG metrics were chosen to match each neural response. Alpha analysis used alpha peak SNR and high-amplitude epoch percentage, where high-amplitude epochs exceeded 150 μV peak-to-peak. Alpha peak SNR was defined as

$$\mathrm{SNR}_{\alpha} = 10 \log_{10} \frac{\bar{P}_{8-12}}{\frac{1}{2}\left(\bar{P}_{6-8} + \bar{P}_{12-14}\right)}, \tag{13}$$

where $\bar{P}_{a-b}$ is the mean PSD in the a–b Hz band. SSVEP analysis used target-plus-harmonic SNR:

$$\mathrm{SNR}_{\mathrm{SSVEP}} = 10 \log_{10} \frac{P(f_{\mathrm{stim}})}{\bar{P}_{\mathcal{N}(f_{\mathrm{stim}})}} + 10 \log_{10} \frac{P(2f_{\mathrm{stim}})}{\bar{P}_{\mathcal{N}(2f_{\mathrm{stim}})}}, \tag{14}$$

where $\bar{P}_{\mathcal{N}(\cdot)}$ is the local neighboring spectral floor within ± 2 Hz, excluding a ± 0.5 Hz guard band. For P300 validation, performance was summarized as Letter@R, the fraction of correctly decoded characters after accumulating R row/column repetitions. The curve-level metric was AUC-rep., defined as the mean Letter@R across repetitions 1–15; Letter@15 was retained as the final-repetition measure.

H. Statistical and Curve Summaries

For the primary benchmark, per-record two-sided Wilcoxon signed-rank tests were Holm-corrected across the 20 reported comparisons (four datasets by five baselines). Varying-SNR curves were summarized by the median artifact-region ΔSNR at each level and by the mean of those 26 medians. Two-sided SPAR-EEG-versus-baseline tests across these curves used three separate Holm families of 130 comparisons (26 SNR levels by five baselines), one per artifact type. Severity-bin tests were two-sided and Holm-corrected across all 45 artifact-type-by-severity-by-baseline comparisons. Because the same source segments were rescaled across SNR levels, these record-level tests characterize paired method differences conditional on the selected source pool and mixture construction; they are not subject-level population inference, and the 26 levels are not independent source cohorts. Exercise EEG inference was performed at the participant level after collapsing O1/O2 and available exercise conditions within participant; two-sided Wilcoxon tests were Holm-corrected across the six primary stress-test outcomes. Exploratory task-wise families are defined in their supplementary table captions. P300 inference was participant-level and used two-sided paired Wilcoxon tests with Holm correction across 12 branch-by-metric comparisons (three denoising branches by four metrics).

IV. Results

The results are organized as artifact-suppression benchmarks, supporting diagnostics, and application-oriented spectral and event-related validations.

TABLE I
MEDIAN ARTIFACT-REGION ΔSNR (DB) ON THE PRIMARY ARTIFACT-SUPPRESSION BENCHMARK. EMG, EOG, AND EOG+EMG ARE EEGDENOISENET -20 DB CONDITIONS; PHYS. DENOTES PHYSIOBANK MOTION.

Method	EMG	EOG	EOG+EMG	Phys.
SPAR-EEG	**17.62**	**17.67**	**17.30**	**19.11**
WQN	16.77	12.71	13.79	17.55
WT-hard	12.69	5.41	7.15	14.24
WT-soft	7.98	1.85	3.67	7.92
EMD-CCA	5.81	4.48	2.59	3.58
EMD-ICA	0.93	2.55	1.00	5.51

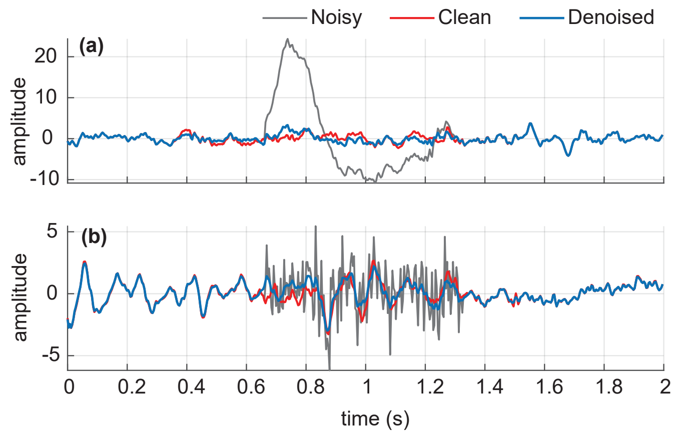

Fig. 2. Representative EEGdenoiseNet examples. Noisy, clean, and SPAR-EEG-denoised waveforms are overlaid for (a) ocular-blink and (b) EMG contamination.

A. Primary Artifact-Suppression Benchmark

The primary benchmark compared WQN, hard and soft wavelet thresholding, EMD-CCA, EMD-ICA, and SPAR-EEG on the controlled EEGdenoiseNet files and the reference-signal PhysioBank motion dataset. Table I reports median artifact-region ΔSNR. At the severe -20 dB EEGdenoiseNet condition, SPAR-EEG produced the largest median improvement among the tested methods for EMG, EOG, and combined EOG+EMG contamination, and also obtained the largest median improvement on PhysioBank.

In paired artifact-region comparisons, SPAR-EEG significantly exceeded all baselines on the three EEGdenoiseNet -20 dB conditions after correction. On PhysioBank, where SPAR-EEG used the slow pass alone, it produced a median improvement of 19.11 dB and significantly exceeded the wavelet and EMD-based baselines; its margin over WQN was not significant (Holm-adjusted $p = 0.198$). Representative EEGdenoiseNet examples show suppression of both ocular and myogenic artifacts while retaining the clean waveform morphology (Fig. 2).

B. EEGdenoiseNet Varying-SNR Benchmark

The varying-SNR benchmark contained 78 EEGdenoiseNet files: 26 integer SNR levels for each of EMG, EOG, and combined EOG+EMG contamination. Figure 3 shows median artifact-region ΔSNR across input SNR. SPAR-EEG had the largest average median improvement among the tested

TABLE II
CURVE-LEVEL SUMMARY OF ARTIFACT-REGION MEDIAN ΔSNR ACROSS 26 EEGDENOISENET SNR LEVELS. VALUES ARE THE MEAN OF THE MEDIAN ΔSNR VALUES ACROSS SNR LEVELS.

Method	EMG	EOG	EOG+EMG
SPAR-EEG	**9.05**	**8.28**	**8.00**
WQN	9.01	6.67	7.11
WT-hard	6.60	2.24	3.38
WT-soft	3.87	0.59	1.65
EMD-CCA	3.92	3.25	1.82
EMD-ICA	1.72	2.18	1.00

comparators for all three artifact families; it closely matched WQN for EMG and showed a clearer advantage for EOG and combined EOG+EMG through most severe and moderate contamination levels.

Table II summarizes each curve by averaging the 26 median ΔSNR values. Among the tested methods, SPAR-EEG achieved the largest average median ΔSNR for all three artifact types, ranking first at 14/26 EMG, 23/26 EOG, and 19/26 EOG+EMG SNR levels.

Record-level two-sided paired Wilcoxon tests were performed at each SNR level, with Holm correction across the 26 levels and five baseline comparisons within each artifact type. Against the artifact-label-guided WQN implementation, SPAR-EEG had a positive median paired ΔSNR difference at 16/26 EMG, 23/26 EOG, and 20/26 EOG+EMG SNR levels; among these, differences were significant after correction at 13/26, 23/26, and 19/26 levels, respectively. WQN-favorable differences were significant at 9/26 EMG, 3/26 EOG, and 6/26 EOG+EMG levels, all within the mild contamination range. Severity-bin comparisons with WQN are reported in Supplementary Table VI.

In the mild severity bin, WQN showed statistically significant but small median advantages for EMG and combined EOG+EMG contamination, whereas SPAR-EEG remained higher for EOG. This pattern may reflect weaker artifact evidence at low severity, where unnecessary preprocessing can reduce downstream ERP/BCI measures [34], [41].

C. SPAR-EEG Pass Ablation

At -10 dB, the combined EMG+EOG sequence produced larger median improvements than either isolated pass for all three EEGdenoiseNet artifact conditions. For EMG contamination, the isolated EMG and EOG passes produced similar median improvements (7.14 dB), but the EMG+EOG sequence increased the median ΔSNR to 10.13 dB. For EOG contamination, the EMG pass alone had little effect, whereas the EOG pass provided most of the improvement. For EOG+EMG contamination, EMG alone partially suppressed the myogenic component, EOG alone suppressed high-amplitude transient structure, and EMG+EOG exceeded both single-pass settings. The slow pass was inactive when used alone on these burst-like EEGdenoiseNet artifacts, but added a small residual gain after EMG+EOG for EOG and EOG+EMG. Full ablation distributions and pass-default settings are reported in Supplementary Tables II and III.

D. Parameter Sensitivity

Sensitivity outcomes changed smoothly around the submitted configuration rather than identifying a single narrow optimum. VMD mode counts of 8 and 12 formed a shallow performance region; the submitted eight-mode setting reduced median runtime by approximately 31% relative to 12 modes and was less invasive outside the artifact mask than four modes. The submitted SSA embedding length of 12 was supported across contamination strengths. VMD suppression was practically stable over proxy thresholds 2–4, whereas the SSA threshold of 3 provided a middle operating point between broader modification at lower thresholds and increasing event bypass at higher thresholds. Removing EOG dilation reduced paired artifact-region ΔSNR by 0.67–2.13 dB, while doubling the margin added only 0.00–0.04 dB and increased outside-mask modification by 2.86–5.75 percentage points. EMG dilation was most beneficial at low contamination, and doubling its submitted margin provided no paired artifact-region benefit. Detailed suppression-preservation results are provided in Supplementary Table XVI and Supplementary Fig. 10.

E. Artifact Geometry and Baseline Availability

For equal one-third artifact support, full-sequence median artifact-region ΔSNR was 10.10 dB for the centered benchmark and 10.12, 10.62, and 10.12 dB for random, left-edge, and right-edge placement, respectively. Three separated bursts with the same total support produced 8.87 dB. In the occupancy sweep, median improvement remained between 9.63 and 10.29 dB through 4/9 occupancy, fell to 3.05 dB at 5/9, and reached 1.50 dB under full-epoch contamination. The fitted two-regime transition and largest median drop both occurred between 4/9 and 5/9 occupancy. Detailed distributions and reconstruction outcomes are provided in Supplementary Tables XVIII–XIX and Supplementary Fig. 12.

F. Runtime and Adaptive Streaming

The full SPAR-EEG sequence was computationally heavier than WQN and wavelet thresholding because of the iterative VMD stage, but remained below real time for single-channel two-second epochs. Median runtime was 84.7 ms for EMG only, 8.9 ms for EOG only, and 95.1 ms for the full sequence, corresponding to a full-sequence real-time factor of 0.048. Detailed computation-cost results are provided in Supplementary Table IV.

Adaptive streaming on PhysioBank produced 3686 full windows across 22 records. The median selected window length was 3.04 s, with an interquartile range of 2.49–3.58 s and a 5th–95th percentile range of 2.08–3.94 s, indicating that the boundary selector used the allowed 2–4 s range. The full epoch-length summary and a representative waveform with adaptive cut points are provided in Supplementary Table V and Supplementary Fig. 4.

G. Task-Locked ERP Preservation

On the independently pre-cleaned ERP recording, the EMG branch was nearly neutral, retaining median mean-amplitude,

This article has been accepted for publication in IEEE Transactions on Neural Systems and Rehabilitation Engineering. This is the author's version which has not been fully edited and content may change prior to final publication. Citation information: DOI 10.1109/TNSRE.2026.3734253

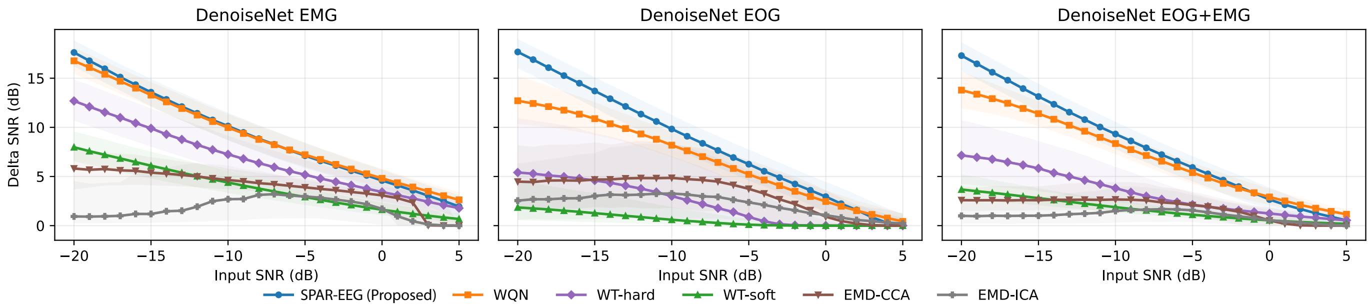

Fig. 3. Artifact-region $\Delta\mathrm{SNR}$ across EEGdenoiseNet input SNR levels. Curves show medians across 3400 epochs; shaded bands indicate interquartile ranges.

aSME, and SME-based SNR values of 99.8%. The EOG branch retained 85.4%, 89.4%, and 95.5%, respectively, identifying it as the main source of attenuation. The full sequence retained 85.5% of mean amplitude, 89.7% of aSME, and 95.3% of SME-based SNR across the 19 channels with reference $|\mathrm{SNR_{SME}}| \geq 5$. Its all-channel signed-SNR profile remained highly similar to the reference ($r = 0.9985$). The slow pass was inactive, so the full and EMG+EOG outputs were identical. Detailed methods, branch-wise results, butterfly ERPs, and signed-SNR maps are provided in Supplementary Section VI.

H. Exercise EEG Spectral Stress-Test Validation

The dry-electrode exercise EEG analysis served as an application-oriented stress test. O1/O2 channels and all available exercise conditions were averaged within participant before group averaging, giving each participant one paired FIR/SPAR-EEG estimate per alpha state or SSVEP frequency. Figure 4 shows a representative movement-contaminated waveform and collapsed spectra.

The collapsed alpha spectra show reduced broadband spectral floor with preserved alpha-band structure. Median alpha peak SNR increased by 1.01 dB in eyes-open blocks and 1.58 dB in eyes-closed blocks; both changes remained significant after Holm correction (Table III). For SSVEP, target-plus-harmonic SNR increased at all four stimulation frequencies, with median improvements of 0.40–1.33 dB. The 7.5, 8.57, and 10 Hz SSVEP rows remained significant after correction, while the 6 Hz row showed a positive but non-significant corrected trend. High-amplitude epoch percentages also decreased from 69.3–93.2% before denoising to 33.8–45.5% after denoising across alpha and SSVEP rows. Because these spectral-prominence metrics are relative measures, uniform amplitude scaling would not increase them; the observed gains indicate that denoising reduced background spectral power more than the task-relevant alpha or SSVEP components. Under the FP1-referenced acquisition, these changes demonstrate improved O1/O2 spectral contrast and may partly reflect attenuation of frontal reference-derived contamination. Task-wise exercise summaries and representative spectra are provided in Supplementary Tables X–XII and Supplementary Figs. 5–7.

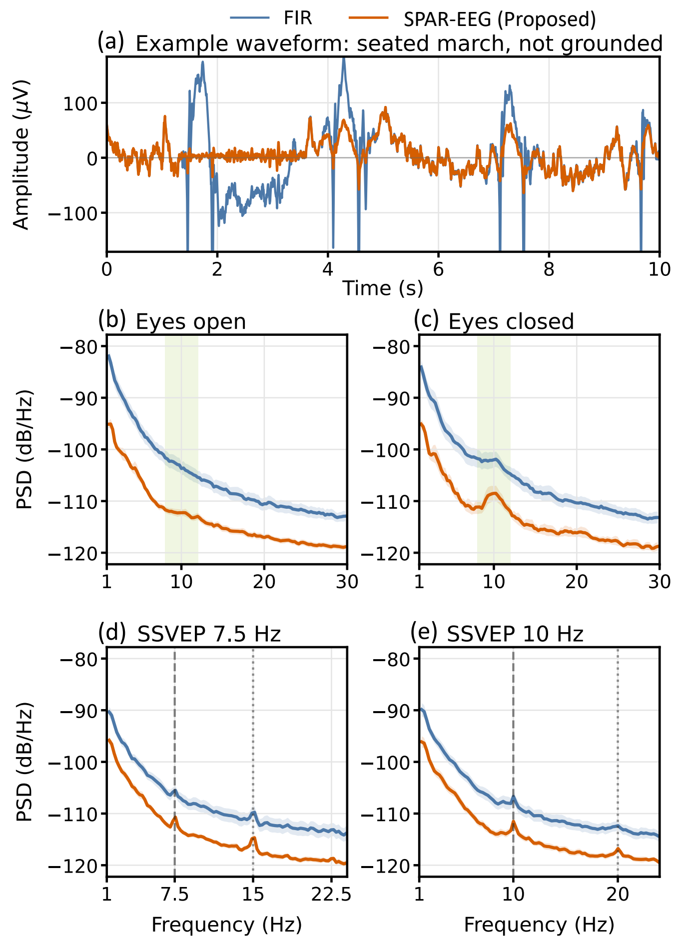

Fig. 4. Exercise EEG example and collapsed spectra. (a) O1 FIR-baseline and SPAR-EEG-denoised waveforms from sub-P008 during eyes-open seated marching under wearable-style/not-grounded acquisition. (b)–(e) Collapsed spectra for eyes-open alpha, eyes-closed alpha, and SSVEP responses at 7.5 and 10 Hz; shaded bands indicate across-subject SEM.

I. P300 BCI Downstream Validation

The P300 BCI validation used all 55 subjects from the Won RSVP/P300 speller dataset with the constrained FP1/FP2 montage. All six P300 runs per subject were processed successfully, giving 1800 training epochs, 5040 test epochs, and 28 decoded test letters per participant. Across repetitions, all denoising branches improved the group mean letter-accuracy curve relative to baseline (Fig. 5); the full sequence increased

TABLE III
COLLAPSED SUBJECT-LEVEL EXERCISE EEG STRESS-TEST SUMMARY FOR ALL PARTICIPANTS ($n = 18$). VALUES SHOW MEDIAN PAIRED CHANGES AFTER DENOISING; p VALUES ARE HOLM-CORRECTED TWO-SIDED WILCOXON TESTS ACROSS THE SIX PRIMARY ROWS. PTP FLAGS SHOW MEDIAN PERCENTAGES OF EPOCHS EXCEEDING 150 μV BEFORE AND AFTER DENOISING.

Domain	Primary metric	Median Δ	Improved	Holm p	PTP flags	Supporting metric, median Δ
Eyes open alpha	Alpha peak SNR	+1.01 dB	77.8%	0.013	93.2%→45.5%	Relative alpha, +1.77 pp
Eyes closed alpha	Alpha peak SNR	+1.58 dB	100.0%	0.000046	69.3%→34.3%	Relative alpha, +3.99 pp
SSVEP 6 Hz	Target+harmonic SNR	+0.40 dB	66.7%	0.081	83.1%→33.8%	Relative target+harmonic, +0.17 pp
SSVEP 7.5 Hz	Target+harmonic SNR	+1.18 dB	94.4%	0.00019	82.5%→34.4%	Relative target+harmonic, +0.14 pp
SSVEP 8.57 Hz	Target+harmonic SNR	+0.89 dB	88.9%	0.0010	86.2%→35.0%	Relative target+harmonic, +0.04 pp
SSVEP 10 Hz	Target+harmonic SNR	+1.33 dB	88.9%	0.0084	89.4%→37.5%	Relative target+harmonic, +0.08 pp

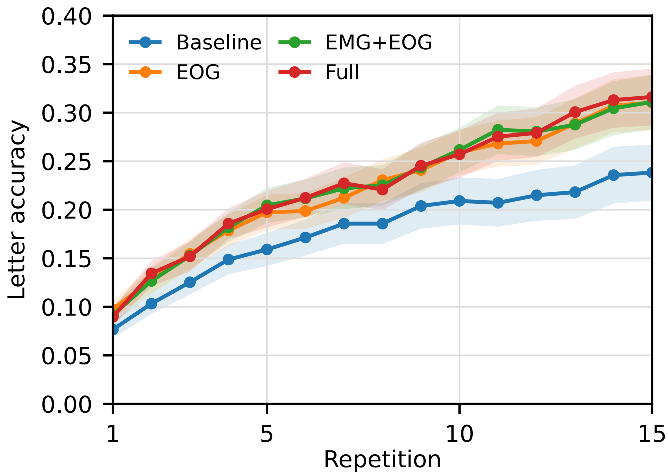

Fig. 5. P300 speller decoding using the FP1/FP2 montage. Curves show participant-level mean letter accuracy across repetitions; shaded bands indicate SEM.

TABLE IV
DOWNSTREAM P300 SPELLER DECODING USING FP1/FP2 ($n = 55$). VALUES ARE PARTICIPANT-LEVEL MEAN ± SEM; HOLM p VALUES CORRESPOND TO AUC-REP. COMPARISONS WITH BASELINE.

Condition	AUC-rep.	ΔAUC	Letter@15	Holm p
Baseline	0.179 ± 0.019	Ref.	0.238 ± 0.029	–
EOG	0.223 ± 0.019	+0.044	0.310 ± 0.029	0.0122
EMG+EOG	0.226 ± 0.019	+0.047	0.311 ± 0.028	0.0063
Full	0.227 ± 0.019	+0.048	0.316 ± 0.029	0.0069

AUC-rep. from 0.179 to 0.227 and improved Letter@15 from 0.238 to 0.316. Table IV reports the corresponding branch-level means and AUC-rep. comparisons.

Paired participant-level comparisons confirmed statistically reliable improvements. For AUC-rep., the EOG, EMG+EOG, and full branches improved over baseline by 0.044, 0.047, and 0.048, respectively, with Holm-corrected two-sided Wilcoxon p values of 0.0122, 0.0063, and 0.0069. At Letter@15, the corresponding improvements were 0.072, 0.073, and 0.078. These gains under the constrained forehead-only montage were obtained with the same decoder protocol and hyperparameters, with separate subject models fitted for each preprocessing branch. Additional P300 metrics and subject-level variability are provided in Supplementary Tables XIV–XV and Supplementary Figs. 8–9.

V. DISCUSSION

This study asked whether a self-contained, artifact-specific single-channel pipeline could suppress diverse artifacts while preserving task-relevant EEG structure. Across the controlled SNR range, SPAR-EEG achieved the largest average improvement among the tested comparators for all three artifact families, although WQN retained small significant advantages for mild EMG and combined EOG+EMG contamination. SPAR-EEG estimated artifact proxies, artifact regions, attenuation strengths, and reconstruction internally. This distinction is important for comparison with WQN, whose benchmark implementation uses known artifact intervals and adjacent uncontaminated segments as reference distributions [19].

Larger gains were observed for EOG and combined EOG+EMG contamination, consistent with using SSA for high-amplitude structured transients whose morphology is not reliably captured by narrowband decomposition alone [4]. For EMG contamination, SPAR-EEG and WQN were closely matched, supporting the VMD pass as an effective treatment for severe and moderate high-frequency bursts. The ablation results further indicate complementary EMG and EOG roles: VMD provides a frequency-informed subspace for muscular bursts, whereas the SSA EOG pass is more variance- and morphology-sensitive and can also suppress high-amplitude EMG-like transients. The implemented EMG+EOG sequence performed most favorably among the tested configurations. The slow pass had a narrower, conditional role: its gate usually bypassed burst-oriented EEGdenoiseNet epochs, whereas the PhysioBank result supports its use for sustained low-frequency contamination. Its modular design permits omission when slow motion or drift is outside the target application.

The sensitivity results further show that the explicit decomposition, detection, and temporal-support controls produce interpretable suppression-preservation and computation trade-offs. The implemented values formed a stable reference configuration within the tested ranges. The one-factor-at-a-time analysis characterized central EMG/EOG controls in isolated passes; interactions among controls, slow-pass settings, and task-specific operating points remain open for further study.

The geometry stress test separates artifact location from within-epoch baseline availability. Random and edge placement produced similar median suppression to centered placement, indicating that the centered benchmark was not uniquely favorable by position. Fragmentation reduced performance moderately, whereas the larger change occurred when occupancy increased from 4/9 to 5/9 and the baseline-dependent

This article has been accepted for publication in IEEE Transactions on Neural Systems and Rehabilitation Engineering. This is the author's version which has not been fully edited and content may change prior to final publication. Citation information: DOI 10.1109/TNSRE.2026.3734253

passes had less uncontaminated support. Full-epoch EMG contamination still showed positive median improvement, but suppression was modest. The observed transition is specific to the tested EMG mixtures, epoch duration, contamination strength, and parameter configuration.

The independently pre-cleaned ERP diagnostic clarifies the preservation tradeoff in neural terms. The EMG branch was nearly neutral, whereas the EOG-containing branches moderately reduced ERP mean amplitude. Measurement error decreased in parallel, so most SME-based ERP SNR and the signed-SNR channel pattern were retained. The inactive slow pass and branch-wise results identify the EOG pass as the main source of attenuation in this recording. As a single-recording analysis, this preservation diagnostic is descriptive.

Computational cost is a second tradeoff: the full sequence was slower than WQN and wavelet thresholding because of the VMD-based EMG pass, but two seconds of single-channel EEG were processed in approximately 95 ms by median runtime. This supports offline and near-real-time monitoring, with further reductions possible through compiled implementations or conditional pass skipping. The adaptive streaming analysis showed that the boundary selector used the 2–4 s range, supporting its role as a continuous-recording wrapper.

The application analyses extend the benchmark evidence beyond reconstruction metrics. In dry-electrode exercise EEG, denoising reduced high-amplitude artifact burden and increased alpha and SSVEP spectral-prominence metrics under movement-prone recording conditions. Because these metrics are relative, the improvements indicate increased spectral contrast rather than a necessary increase in absolute neural amplitude. Accordingly, these findings represent improved spectral prominence under the acquired FP1-referenced montage and may partly reflect attenuation of frontal reference-derived contamination. In the P300 speller analysis, denoising improved the repetition-accuracy curve and final-repetition accuracy using only FP1 and FP2, with similar gains for the EOG, EMG+EOG, and full-sequence branches. This suggests that frontal ocular and facial artifact suppression was the dominant contributor in that montage, a setting relevant to low-burden assistive and rehabilitation-oriented wearable EEG [1].

Several limitations remain. The EMG and EOG passes benefit from relatively clean baseline samples within the epoch, and the slow pass may leave residual low-frequency artifact when the estimated component is ambiguous. Legitimate neural transients that resemble the targeted artifact morphology may also be attenuated, as reflected by the moderate EOG-related amplitude reduction in the ERP preservation diagnostic. The full sequence is computationally heavier than lightweight wavelet and WQN baselines, although runtime remained below real time. Performance relative to modern neural denoisers remains unestablished. The exercise validation relies on surrogate spectral metrics from one FP1-referenced acquisition configuration rather than clean EEG, and the P300 validation tests one event-related BCI paradigm under a constrained FP1/FP2 montage.

VI. Conclusion

This paper introduced SPAR-EEG, a self-contained single-channel EEG denoising framework whose central mechanism regularizes artifact-dominant component regions toward a within-window baseline rather than rejecting complete components. Artifact-specific VMD and SSA passes implement this mechanism for high-frequency EMG bursts and blink-like ocular transients, followed by a separately gated SSA slow-drift module. Across controlled EEGdenoiseNet benchmarks, it obtained the largest average artifact-region SNR improvement among the tested baselines for EMG, EOG, and combined EOG+EMG contamination. Pass ablation showed complementary EMG and EOG roles, while a low-artifact ERP diagnostic showed that most task-locked detectability was retained.

The application analyses suggest that the same preprocessing can improve task-relevant EEG usability beyond direct reconstruction metrics. In dry-electrode exercise EEG, denoising reduced high-amplitude artifact burden and increased alpha and SSVEP spectral-prominence metrics. In a public RSVP/P300 speller dataset using only FP1 and FP2, denoising increased repetition-curve AUC by 0.048 and improved common-protocol Letter@15 accuracy by 7.8 percentage points. These properties are relevant to low-burden assistive and rehabilitation-oriented EEG applications, where limited channels, movement, and weak supervision constrain preprocessing. Overall, the results support artifact-specific gating and selective attenuation as a practical self-contained alternative to guided or globally applied single-channel denoising. Future work will optimize implementation, adaptive pass triggering, and validation in additional long-duration wearable and clinical monitoring datasets.

Ethics Statement

The dry-electrode exercise EEG study was approved by the Auckland University of Technology Ethics Committee (AUTEC application 24/325; approved 13 November 2025), and all participants provided informed consent.

Data and Code Availability

Code and reproducibility materials are available at https://github.com/usmanqamarshaikh/SPAR-EEG. The repository includes the EEGdenoiseNet and PhysioBank comparison workflows, parameter-sensitivity and artifact-geometry analyses, the EEGLAB ERP-preservation diagnostic, the RSVP/P300 BCI validation workflow, and demonstrations for applying SPAR-EEG to EEGLAB data structures and related single-channel EEG workflows. EEGdenoiseNet, PhysioBank, the EEGLAB sample recording, and the RSVP/P300 dataset are publicly available from their original sources. The dry-electrode exercise EEG dataset cannot be publicly released at this stage.

References

[1] R. Abiri, S. Borhani, E. W. Sellers, Y. Jiang, and X. Zhao, "A comprehensive review of EEG-based brain-computer interface paradigms," *Journal of Neural Engineering*, vol. 16, no. 1, p. 011001, 2019.

[2] F. Sauvet, C. Bougard, M. Coroenne, L. Lely, P. V. Beers, M. Elbaz, M. Guillard, D. Leger, and M. Chennaoui, "In-flight automatic detection of vigilance states using a single EEG channel," *IEEE Transactions on Biomedical Engineering*, vol. 61, no. 12, pp. 2840–2847, 2014.

[3] T. Elbert, W. Lutzenberger, B. Rockstroh, and N. Birbaumer, "Removal of ocular artifacts from the EEG: A biophysical approach to the EOG," *Electroencephalography and Clinical Neurophysiology*, vol. 60, no. 5, pp. 455–463, 1985.

[4] A. K. Maddirala and K. C. Veluvolu, "Eye-blink artifact removal from single channel EEG with k-means and SSA," *Scientific Reports*, vol. 11, no. 1, p. 11043, 2021.

[5] M. Chavez, F. Grosselin, A. Bussalb, F. D. V. Fallani, and X. Navarro-Suné, "Surrogate-based artifact removal from single-channel EEG," *IEEE Transactions on Neural Systems and Rehabilitation Engineering*, vol. 26, no. 3, pp. 540–550, 2018.

[6] S. D. Fickling, C. C. Liu, R. C. N. D'Arcy, S. G. Hajra, and X. Song, "Good data? the EEG quality index for automated assessment of signal quality," in *2019 IEEE 10th Annual Information Technology, Electronics and Mobile Communication Conference*, 2019, pp. 219–229.

[7] R. Vigario, J. Sarela, V. Jousmiki, M. Hamalainen, and E. Oja, "Independent component approach to the analysis of EEG and MEG recordings," *IEEE Transactions on Biomedical Engineering*, vol. 47, no. 5, pp. 589–593, 2000.

[8] M. A. Uusitalo and R. J. Ilmoniemi, "Signal-space projection method for separating MEG or EEG into components," *Medical and Biological Engineering and Computing*, vol. 35, no. 2, pp. 135–140, 1997.

[9] C.-Y. Chang, S.-H. Hsu, L. Pion-Tonachini, and T.-P. Jung, "Evaluation of artifact subspace reconstruction for automatic EEG artifact removal," in *2018 40th Annual International Conference of the IEEE Engineering in Medicine and Biology Society*, 2018, pp. 1242–1245.

[10] G. Gratton, M. G. H. Coles, and E. Donchin, "A new method for off-line removal of ocular artifact," *Electroencephalography and Clinical Neurophysiology*, vol. 55, no. 4, pp. 468–484, 1983.

[11] P. He, G. Wilson, and C. Russell, "Removal of ocular artifacts from electro-encephalogram by adaptive filtering," *Medical and Biological Engineering and Computing*, vol. 42, no. 3, pp. 407–412, 2004.

[12] H. Zhang, M. Zhao, C. Wei, D. Mantini, Z. Li, and Q. Liu, "EEG-denoiseNet: A benchmark dataset for deep learning solutions of EEG denoising," *Journal of Neural Engineering*, vol. 18, no. 5, p. 056057, 2021.

[13] J. Chen, D. Pi, X. Jiang, Y. Xu, Y. Chen, and X. Wang, "Denosieformer: A transformer-based approach for single-channel EEG artifact removal," *IEEE Transactions on Instrumentation and Measurement*, vol. 73, pp. 1–16, 2024.

[14] J. Yin, A. Liu, C. Li, R. Qian, and X. Chen, "A GAN guided parallel CNN and transformer network for EEG denoising," *IEEE Journal of Biomedical and Health Informatics*, vol. 29, no. 6, pp. 3930–3941, 2025.

[15] S. G. Mallat, "A theory for multiresolution signal decomposition: The wavelet representation," *IEEE Transactions on Pattern Analysis and Machine Intelligence*, vol. 11, no. 7, pp. 674–693, 1989.

[16] S. Khatun, R. Mahajan, and B. I. Morshed, "Comparative study of wavelet-based unsupervised ocular artifact removal techniques for single-channel EEG data," *IEEE Journal of Translational Engineering in Health and Medicine*, vol. 4, pp. 1–8, 2016.

[17] H. Peng, B. Hu, Q. Shi, M. Ratcliffe, Q. Zhao, Y. Qi, and G. Gao, "Removal of ocular artifacts in EEG: An improved approach combining DWT and ANC for portable applications," *IEEE Journal of Biomedical and Health Informatics*, vol. 17, no. 3, pp. 600–607, 2013.

[18] M. K. Islam, P. Ghorbanzadeh, and A. Rastegarnia, "Probability mapping based artifact detection and removal from single-channel EEG signals for brain-computer interface applications," *Journal of Neuroscience Methods*, vol. 360, p. 109249, 2021.

[19] M. Dora and D. Holcman, "Adaptive single-channel EEG artifact removal with applications to clinical monitoring," *IEEE Transactions on Neural Systems and Rehabilitation Engineering*, vol. 30, pp. 286–295, 2022.

[20] N. E. Huang, Z. Shen, S. R. Long, M. C. Wu, H. H. Shih, Q. Zheng, N.-C. Yen, C. C. Tung, and H. H. Liu, "The empirical mode decomposition and the Hilbert spectrum for nonlinear and non-stationary time series analysis," *Proceedings of the Royal Society of London. Series A: Mathematical, Physical and Engineering Sciences*, vol. 454, no. 1971, pp. 903–995, 1998.

[21] M. E. Torres, M. A. Colominas, G. Schlotthauer, and P. Flandrin, "A complete ensemble empirical mode decomposition with adaptive noise," in *Proceedings of the 2011 IEEE International Conference on Acoustics, Speech and Signal Processing*, 2011, pp. 4144–4147.

[22] K. T. Sweeney, S. F. McLoone, and T. E. Ward, "The use of ensemble empirical mode decomposition with canonical correlation analysis as a novel artifact removal technique," *IEEE Transactions on Biomedical Engineering*, vol. 60, no. 1, pp. 97–105, 2013.

[23] C. M. Sweeney-Reed, S. J. Nasuto, M. F. Vieira, and A. O. Andrade, "Empirical mode decomposition and its extensions applied to EEG analysis: A review," *Advances in Data Science and Adaptive Analysis*, vol. 10, no. 2, p. 1840001, 2018.

[24] X. Chen, C. He, and H. Peng, "Removal of muscle artifacts from single-channel EEG based on ensemble empirical mode decomposition and multiset canonical correlation analysis," *Journal of Applied Mathematics*, vol. 2014, no. 1, p. 261347, 2014.

[25] Q. Li, L. Wei, Y. Xu, and B. Yang, "Ocular artifact removal algorithm of single channel EEG based on CEEMDAN-ICA-WTD," in *2021 IEEE 6th International Conference on Signal and Image Processing*, 2021, pp. 451–455.

[26] Q. Wu, W. Zhang, Y. Wang, W. Zhang, and X. Liu, "Research on removal algorithm of EOG artifacts in single-channel EEG signals based on CEEMDAN-BD," *Computer Methods in Biomechanics and Biomedical Engineering*, vol. 24, no. 12, pp. 1368–1379, 2021.

[27] K. Dragomiretskiy and D. Zosso, "Variational mode decomposition," *IEEE Transactions on Signal Processing*, vol. 62, no. 3, pp. 531–544, 2014.

[28] C. Liu and C. Zhang, "Remove artifacts from a single-channel EEG based on VMD and SOBI," *Sensors*, vol. 22, no. 17, p. 6698, 2022.

[29] M. Saini, Payal, and U. Satija, "An effective and robust framework for ocular artifact removal from single-channel EEG signal based on variational mode decomposition," *IEEE Sensors Journal*, vol. 20, no. 1, pp. 369–376, 2020.

[30] C. Dora and P. K. Biswal, "An improved algorithm for efficient ocular artifact suppression from frontal EEG electrodes using VMD," *Biocybernetics and Biomedical Engineering*, vol. 40, no. 1, pp. 148–161, 2020.

[31] M. S. Hossain, M. B. I. Reaz, M. E. H. Chowdhury, S. H. M. Ali, A. A. A. Bakar, S. Kiranyaz, A. Khandakar, M. Alhatou, and R. Habib, "Motion artifacts correction from EEG and fNIRS signals using novel multiresolution analysis," *IEEE Access*, vol. 10, pp. 29 760–29 777, 2022.

[32] J. Cheng, L. Li, C. Li, Y. Liu, A. Liu, R. Qian, and X. Chen, "Remove diverse artifacts simultaneously from a single-channel EEG based on SSA and ICA: A semi-simulated study," *IEEE Access*, vol. 7, pp. 60 276–60 289, 2019.

[33] S. K. Noorbasha and G. F. Sudha, "Hybrid algorithm for multi artifact removal from single channel EEG," *Biomedical Physics and Engineering Express*, vol. 7, no. 4, p. 045003, 2021.

[34] U. Q. Shaikh, A. M. Kalra, A. Lowe, and I. K. Niazi, "Multi-head noise regression for single-channel EEG: Estimating ocular and muscle contamination to guide artifact removal," *Journal of Neural Engineering*, vol. 23, no. 2, p. 026024, 2026.

[35] K. Won, M. Kwon, M. Ahn, and S. C. Jun, "EEG dataset for RSVP and P300 speller brain-computer interfaces," *Scientific Data*, vol. 9, p. 388, 2022.

[36] K. T. Sweeney, H. Ayaz, T. E. Ward, M. Izzetoglu, S. F. McLoone, and B. Onaral, "A methodology for validating artifact removal techniques for physiological signals," *IEEE Transactions on Information Technology in Biomedicine*, vol. 16, no. 5, pp. 918–926, 2012.

[37] A. Delorme and S. Makeig, "Eeglab: An open source toolbox for analysis of single-trial eeg dynamics including independent component analysis," *Journal of Neuroscience Methods*, vol. 134, no. 1, pp. 9–21, 2004.

[38] L. Pion-Tonachini, K. Kreutz-Delgado, and S. Makeig, "ICLabel: An automated electroencephalographic independent component classifier, dataset, and website," *NeuroImage*, vol. 198, pp. 181–197, 2019.

[39] S. J. Luck, A. X. Stewart, A. M. Simmons, and M. Rhemtulla, "Standardized measurement error: A universal metric of data quality for averaged event-related potentials," *Psychophysiology*, vol. 58, no. 6, p. e13793, 2021.

[40] W. Zhang and E. S. Kappenman, "Maximizing signal-to-noise ratio and statistical power in ERP measurement: Single sites versus multi-site average clusters," *Psychophysiology*, vol. 61, no. 2, p. e14440, 2024.

[41] A. Delorme, "EEG is better left alone," *Scientific Reports*, vol. 13, no. 1, p. 2372, 2023.